

ENGIN-X: a third-generation neutron strain scanner

J. R. Santisteban, M. R. Daymond, J. A. James and L. Edwards

Copyright © International Union of Crystallography

Author(s) of this paper may load this reprint on their own web site provided that this cover page is retained. Republication of this article or its storage in electronic databases or the like is not permitted without prior permission in writing from the IUCr.

ENGIN-X: a third-generation neutron strain scanner

J. R. Santisteban,^{a*‡} M. R. Daymond,^{a¶} J. A. James^b and L. Edwards^b

^aISIS Facility, Rutherford Appleton Laboratory, CCLRC, Chilton, Didcot, OX11 0QX, UK, and
^bDepartment of Materials Engineering, The Open University, Milton Keynes, MK7 6AA, UK.
Correspondence e-mail: jrsantisteban@cab.cnea.gov.ar

ENGIN-X, a new time-of-flight (TOF) neutron diffractometer optimized to measure elastic strains at precise locations in bulky specimens recently commissioned at the ISIS Facility in the Rutherford Laboratory, UK, is described. Fast counting times, together with a flexible and accurate definition of the instrumental gauge volume are the main requirements of neutron strain scanning and have been addressed on ENGIN-X through the design of a novel TOF diffractometer with a tuneable resolution and interchangeable radial collimators. Further, the routine operation of the instrument has been optimized by creating a virtual instrument, *i.e.* a three-dimensional computer representation of the diffractometer and samples, which assists in the planning and execution of experiments. On comparing ENGIN-X with its predecessor ENGIN, a 25× gain in performance is found, which has allowed the determination of stresses up to 60 mm deep in steel specimens. For comparison with constant-wavelength diffractometers, special attention has been paid to the absolute number of counts recorded during the experiments. A simple expression is presented for the estimation of counting times in TOF neutron strain scanning experiments.

© 2006 International Union of Crystallography
Printed in Great Britain – all rights reserved

1. Introduction

Neutron strain scanning (NSS) is a non-destructive technique that provides insights into strain and stress fields deep within engineering components and structures (Allen *et al.*, 1985). The popularity and maturity of NSS is reflected in a series of recent publications. An ISO standard dealing with residual stress measurement by neutron diffraction has been proposed in ISO/TTA 3:2001 (2001). A comprehensive introduction to the technique is found in the book by Hutchings *et al.* (2005), and a description of the state-of-the-art of stress measurements using neutron and synchrotron radiation is given in the book by Fitzpatrick & Lodini (2003).

The technique was first developed in the late 1970s on conventional ‘all-purpose’ diffractometers. The technique developed significantly over the following two decades with an increase in the user community, and a number of neutron diffractometers were converted to work almost entirely for NSS. ISIS, the world’s brightest pulsed neutron source, was home to one of the first dedicated neutron stress diffractometers, ENGIN (Johnson *et al.*, 1997). Following increased demand from the engineering community, ENGIN has recently been replaced by ENGIN-X (Daymond & Edwards, 2004), which was designed to provide at least an order of

magnitude improvement in performance (Johnson & Daymond, 2002).

Second-generation neutron strain scanners were built on diffractometers originally designed to balance the competing requirements of various experiment types. This limited their utility for engineering measurements, particularly in large components. In contrast, ENGIN-X has been designed with the sole aim of making engineering strain measurements: essentially the accurate measurement of polycrystalline material lattice parameters, at a precisely determined location in an object. This approach has allowed considerable performance improvements to be made compared with previous instrumentation.

Here we describe ENGIN-X, providing a precise quantification of the gain in performance achieved through optimized neutron optics. In addition, we introduce a virtual laboratory: a computing representation of ENGIN-X designed to assist in the planning and execution of experiments.

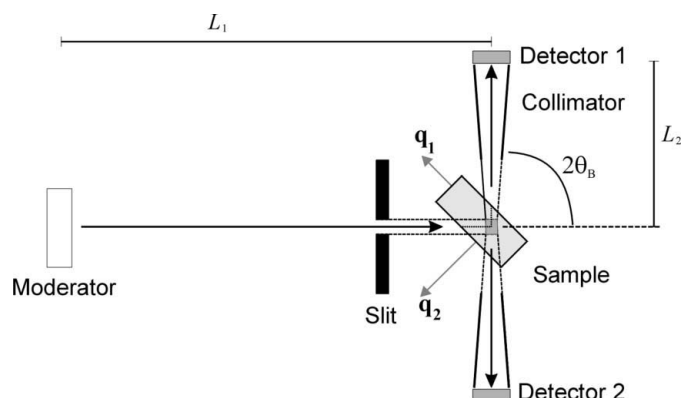
2. An optimized time-of-flight neutron strain scanner

2.1. Basic concepts

The aim of a time-of-flight (TOF) neutron strain scanner is to define the macroscopic elastic strain tensor at definite locations in the bulk of a specimen; a schematic is shown in Fig. 1. A pulsed beam of neutrons with a wide energy range travels to the sample, where a small fraction of the beam is

[‡] Now at: Laboratorio de Física de Neutrones, Centro Atómico Bariloche, Bariloche, Argentina.

[¶] Now at: Department of Mechanical and Materials Engineering, Queen’s University, Kingston, ON K7L 3N6, Canada.


Figure 1

Schematic diagram of a time-of-flight neutron strain scanner. The elastic strain is measured along the directions of the impulse exchange vector, \mathbf{q}_1 and \mathbf{q}_2 . The volume of the sample explored by the instrument corresponds to the intersection of incident and diffracted beams, as defined by slits and collimators.

scattered into a detector at an angle $2\theta_B$. Assuming an elastic collision, the wavelength of the detected neutrons is defined from its TOF t ,

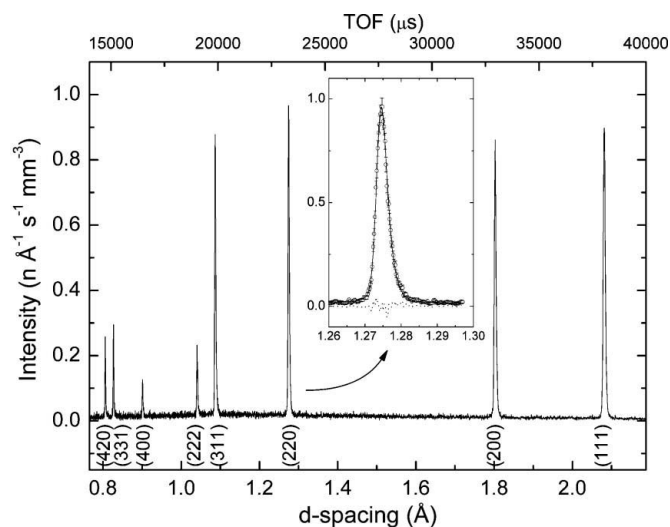
$$\lambda = \frac{h}{m(L_1 + L_2)t}, \quad (1)$$

with h being Planck's constant, m the neutron mass and L_1 and L_2 the primary and secondary flight paths, respectively. A typical spectrum diffracted by a polycrystalline material is shown in Fig. 2. Each peak corresponds to an (hkl) family of lattice planes as given by Bragg's law, $\lambda_{hkl} = 2d_{hkl} \sin \theta_B$, so the d -spacing is obtained from the position t_{hkl} of the peak in the TOF spectrum,

$$d_{hkl} = \frac{h}{2 \sin \theta_B m (L_1 + L_2) t_{hkl}}. \quad (2)$$

Peak positions can be precisely determined by least-squares refinement of the peaks, with a typical sensitivity of $\delta\varepsilon = \Delta t_{hkl}/t_{hkl} = \Delta d_{hkl}/d_{hkl} \simeq 50 \mu\varepsilon$ ($1 \mu\varepsilon = 10^{-6}$). The elastic strain is determined from the change in the atomic interplanar distances d_{hkl} , as compared with the value d_{hkl}^0 measured in the unstressed (or reference) condition, $\varepsilon_{hkl} = (d_{hkl} - d_{hkl}^0)/d_{hkl}^0$. Each diffraction peak provides information from only a small fraction of the crystallites within the sampled volume, *i.e.* those oriented to fulfil the Bragg condition. A good approximation to the macroscopic or 'engineering' elastic strain is usually given by a weighted average of several single-peak strains ε_{hkl} (Kamminga *et al.*, 2000). In TOF instruments, the engineering strain can also be approximated from the change in the average lattice parameters from Rietveld or Pawley refinements of the complete diffraction spectrum (Daymond *et al.*, 1997; Daymond, 2004).

The volume of material contributing to the diffraction pattern corresponds to the intersection of the incident and diffracted beams, typically defined by slits and collimators, respectively. As neutrons penetrate quite deeply into most materials, strains within the bulk of a specimen can be non-destructively measured. The centroid of this gauge volume


Figure 2

Typical TOF diffraction spectrum on ENGIN-X, in this case for a stainless-steel specimen. The elastic strain is calculated from the shift in the peak positions defined through a least-squares refinement (inset). The macroscopic strain is obtained from the change in lattice parameter given by a full-pattern refinement.

(typically of the order of cubic millimetres) defines the location of the measurement. In an NSS instrument, the gauge volume is fixed at a position in the laboratory, so the strain variation across the sample is explored by moving the sample using a translation stage.

The measured strain gives the component of the strain tensor along the direction of the neutron wavevector change \mathbf{q} , which bisects the incident and diffracted beams (Fig. 1). A complete definition of the strain tensor for an unknown specimen requires measuring at least six non-coplanar directions. However, the principal strain axes can usually be inferred from the geometry of the sample, and measurements are performed only along three mutually perpendicular directions. In order to ensure that the same volume of the specimen is measured for each sample orientation, the detector is placed at approximately 90° from the incident beam, defining a near cubic gauge volume. Two perpendicular strain directions can be measured simultaneously during TOF NSS by adding a second detector opposite to the first one, aligned such that the same gauge volume is seen from both detectors.

The NSS technique is conceptually very simple but its practical application can be time-consuming. Very long counting times are required when small gauge volumes and large penetration depths are involved, which effectively dictates the range of problems that can be studied with this technique. Withers (2004) has defined a 'maximum acceptable acquisition time' for neutron and synchrotron strain scanning when measuring strain deep within materials. This is an important concept because NSS experiments are performed at large facilities, where the experimenter is granted a limited amount of beam time, under competitive review. Hence, a minimization of the experimental time required for an accurate determination of peak positions (and hence strain) is the first goal of an optimized strain scanner.

Further, a precise knowledge of the location of the gauge volume within the sample is paramount to NSS experiments. An international round robin for the standardization of NSS (Webster, 2000; Daymond *et al.*, 2001) unexpectedly revealed that one of the main sources of differences between the participating laboratories resulted from positioning errors, rather than from uncertainties in the determination of interplanar distances. Aligning a specimen is relatively easy for simple geometries such as plates or cylinders, but it is non-trivial with real components presenting more complex shapes. As a result, the time spent on alignments often represents an important fraction of allocated beam time. Thus, a second aim for an optimized neutron strain scanner is a precise yet flexible definition of the instrumental gauge volume, ideally in conjunction with fast and accurate alignment procedures.

2.2. Counting time for a TOF neutron strain scanner

The uncertainty in the measured strain is proportional to the uncertainty in the determination of the position of the Bragg peaks. Withers *et al.* (2001) have shown that the time T required to measure the position of an arbitrary shaped peak on zero-background with a strain precision $\delta\varepsilon$ is

$$T = \frac{1}{I_{hkl}} \left(\frac{\delta t_{hkl}}{t_{hkl} \delta\varepsilon} \right)^2 = \frac{1}{I_{hkl}} \left(\frac{\delta_\varepsilon t_{hkl}}{\delta\varepsilon} \right)^2, \quad (3)$$

where I_{hkl} is the integrated peak intensity per unit time, t_{hkl} is the peak position and δt_{hkl} the peak width. The inverse of T can be used as a figure of merit for the purpose of optimizing a neutron strain scanner (Johnson & Daymond, 2002). On the right-hand side of equation (3), T is expressed in terms of the relative peak width $\delta_\varepsilon t_{hkl} = (\delta t_{hkl}/t_{hkl})$: a dimensionless parameter that allows direct comparison between peaks appearing at different TOF, as well as with the required strain precision $\delta\varepsilon$. Throughout this paper the notation $\delta_\varepsilon X$ will be used to represent the dimensionless relative width of the probability distribution of the variable X .

The relative peak width, or resolution, of a TOF diffractometer is (Windsor, 1981)

$$(\delta_\varepsilon t_{hkl})^2 = (\delta_\varepsilon t)_{\text{mod}}^2 + \frac{\cot^2 \theta_B}{4} [(\alpha_{\text{in}}^x)^2 + (\alpha_{\text{det}}^z)^2] + (\delta_\varepsilon d_{hkl})^2, \quad (4)$$

where $(\delta_\varepsilon t)_{\text{mod}}$ is the moderator contribution to the resolution, α_{in}^x and α_{det}^z are the divergence in the diffraction plane for the incident and detected beams, respectively, and $(\delta_\varepsilon d_{hkl})$ is the sample-induced broadening appearing from microstresses or gradients in composition (Snyder *et al.*, 1999). The divergence perpendicular to the diffraction plane does not affect the peak width.

The moderator contribution to the peak width is a crucial characteristic of a TOF diffractometer, as it usually dictates the overall resolution of the instrument. It represents the time distribution of the neutron pulse due to the neutron thermalization process. Its shape and dependence on neutron wavelength has been extensively discussed by Ikeda & Carpenter (1985). Its contribution to the resolution is inversely proportional to the total neutron flight path $L = L_1 + L_2$,

$$(\delta_\varepsilon t)_{\text{mod}}^2 = \left[\frac{h \Delta t_0}{(L_1 + L_2) m \lambda} \right]^2, \quad (5)$$

where Δt_0 is the intrinsic width of the neutron pulse: a measure of the time spent by the neutrons in the moderator.

The integrated intensity of a TOF diffraction peak (Buras, 1963) depends on the scattering power and absorption of the sample as well as on instrumental parameters, such as the incident neutron flux Φ_0 (expressed in neutrons $\text{s}^{-1} \text{cm}^{-2} \text{\AA}^{-1} \text{steradian}^{-1}$), the total divergence in the diffraction plane, the incident-beam divergence perpendicular to the diffraction plane α_{in}^y , the size of the illuminated gauge volume δV , and the detector characteristics:

$$I_{hkl} = \Phi_0 \alpha_{\text{in}}^y \left(\frac{h_{\text{det}} \%_{\text{det}}}{\pi L_2} \right) \sin \theta_B [(\alpha_{\text{in}}^x)^2 + (\alpha_{\text{det}}^z)^2]^{1/2} \times P_{hkl} \exp(-l \mu_{hkl}) \delta V, \quad (6)$$

where h_{det} and $\%_{\text{det}}$ are the detector height and efficiency, respectively. The beam attenuation is given by the absorption coefficient μ_{hkl} , and l , the total flight path inside the sample indicated by the dotted line in Fig. 1. The factor P_{hkl} depends only on the material,

$$P_{hkl} = \frac{m_{hkl} |F_{hkl}^2| d_{hkl}^4}{v_0}, \quad (7)$$

with v_0 the volume per atom, F_{hkl}^2 the structure factor (including the Debye–Waller factor) and m_{hkl} the multiplicity of the reflection. A precise definition of the illuminated gauge volume δV is given in the next section.

Thus the counting time required to achieve a $\delta\varepsilon$ uncertainty in strain, expressed in terms of the experimental parameters, is

$$T = \frac{\exp(l \mu_{hkl}) \pi L_2}{(\delta\varepsilon)^2} \times \frac{(\delta_\varepsilon t)_{\text{mod}}^2 + (\cot^2 \theta_B / 4) [(\alpha_{\text{in}}^x)^2 + (\alpha_{\text{det}}^z)^2] + (\delta_\varepsilon d_{hkl})^2}{\alpha_{\text{in}}^y \delta V \Phi_0 P_{hkl} h_{\text{det}} \%_{\text{det}} \sin \theta_B [(\alpha_{\text{in}}^x)^2 + (\alpha_{\text{det}}^z)^2]^{1/2}}. \quad (8)$$

This expression gives some guidelines for the design of a TOF neutron strain scanner. Fig. 3(a) shows the dependence of T on the horizontal incident-beam divergence α_{in}^x , for different divergences of the diffracted beam. The calculations are for the case of negligible sample broadening ($\delta_\varepsilon d_{hkl} = 0$) and $\delta_\varepsilon t_{\text{mod}} = 0.001$. For small divergences of the diffracted beam ($\alpha_{\text{det}}^z = 0.0005$), a minimum exists at $\alpha_{\text{in}}^x \simeq 0.002$, *i.e.* twice the moderator broadening. As the detector collimation is relaxed ($\alpha_{\text{det}}^z = 0.001, 0.002$), the minimum shifts to lower incident-beam divergences, and the counting time increases. The condition for the minimum is

$$\frac{\cot^2 \theta_B}{4} [(\alpha_{\text{in}}^x)^2 + (\alpha_{\text{det}}^z)^2] = (\delta_\varepsilon t)_{\text{mod}}^2 + (\delta_\varepsilon d_{hkl})^2. \quad (9)$$

Thus, in an optimized instrument, the angular contribution to the resolution must match the combined contributions from moderator and sample: a principle usually adopted in instrument design (Windsor, 1981). This means that the resolution of an optimized instrument is ultimately determined by

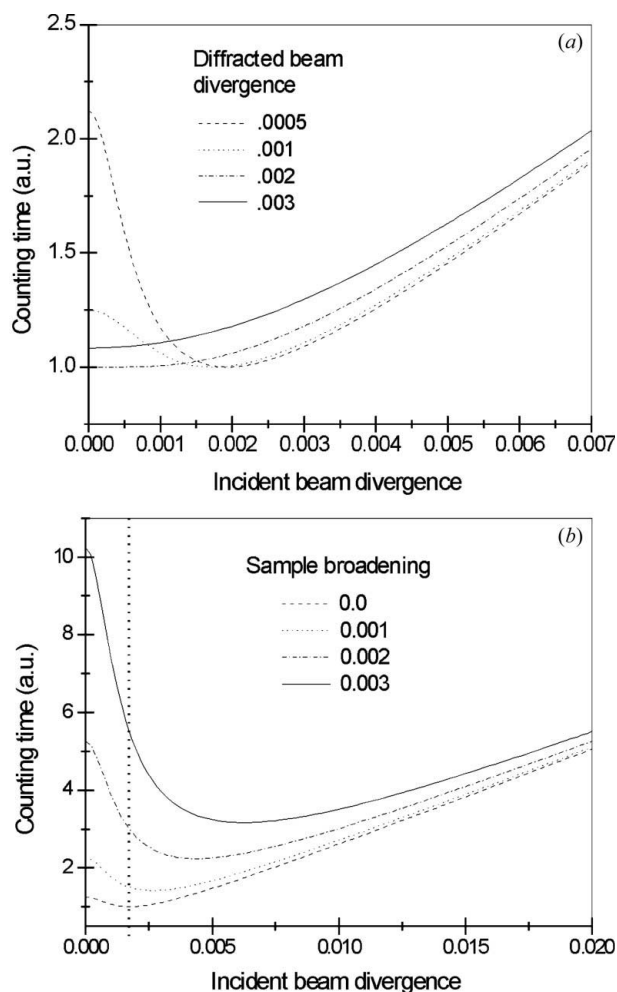


Figure 3 Counting time required to achieve a predefined strain uncertainty versus the incident-beam divergence in the diffraction plane. (a) Predictions for different diffracted-beam divergences, for a sample giving a negligible broadening. (b) Predictions for different sample-induced broadenings, for a diffracted-beam divergence of 0.002.

the moderator contribution $(\delta_{\epsilon t})_{\text{mod}}$, *i.e.* by the choice of moderator and total flight path. However, the sample broadening should also be taken into account at the design stage. This can be seen in Fig. 3(b), showing the increase in counting times due to sample-induced broadening. As indicated by the vertical dotted line, an instrument having an incident divergence optimized for a negligible sample broadening would become rather inefficient for samples presenting broad peaks, because counting times increase quite sharply for highly collimated incident beams. Therefore, this calls for an instrument with a variable divergence, which can be adjusted to match the peak broadening introduced by the sample, since typically the incident flux can be increased if we are willing to increase the divergence. In practical terms, the moderator contribution to the resolution is minimized by the choice of moderator and a long incident flight path. Increasing the secondary flight path L_2 is not effective because there is an associated decay in intensity of the form $(1/L_2)^2$. By contrast, the loss of neutrons caused by increasing L_1 can be kept relatively low by bringing the neutrons along a neutron guide.

The actual choice of L_1 will depend on a variety of parameters, including building costs and the materials likely to be studied with the diffractometer.

2.3. The gauge volume in a TOF neutron strain scanner

The measured strain corresponds to an average over the volume δV and solid angle $\delta\Omega$ sampled. The instrument gauge volume (IGV) is the volume of space defined by the neutron beam paths through the defining apertures, taking into account the beam intensity profile and divergence. Fig. 4(a) schematically shows the main experimental parameters affecting the shape and size of the IGV. The cross section of the neutron beam is defined by slits of height S_y and width S_x located at a distance S_z from the geometric centre of the diffractometer. The incident beam has a divergence α_{in}^x in the diffraction plane and α_{in}^y perpendicular to it. Due to this divergence, the beam cross section is larger at the IGV centre than at the slits and hence the edges of the IGV are blurred. The edge profile is described by an error function, with a width defined by the divergence and slit distance. Withers *et al.* (2000) have shown that the full width at half-maximum (FWHM) of the incident-beam profile at the IGV centre is

$$\Delta x, y = S_{x,y} \left[1 + 2.35 \left(\frac{S_z}{S_{x,y}} \tan \alpha_{x,y} \right)^3 \right]^{1/3}. \quad (10)$$

Hence, the effective dimensions of the beam, as defined by the FWHM, increase slowly with the slit distance S_z , even when the actual cross section of the beam increases markedly.

The size of the IGV along the beam direction Δz is usually defined by a collimator. According to equation (9), an instrument with a moderator resolution of 0.001 requires a diffracted beam with a divergence $\alpha_{\text{det}}^z \simeq 0.002$ radians in the

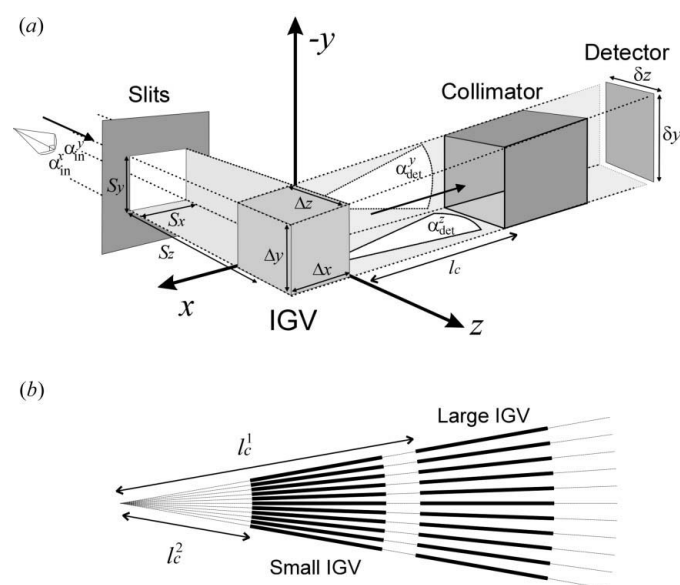


Figure 4 (a) The instrumental gauge volume (IGV) in TOF neutron strain scanning, identifying the parameters defining its shape and dimension. (b) Design of two radial collimators having the same divergence but different spatial resolutions.

diffraction plane. For detectors located at a secondary flight path of 1.5 m, this gives a detector width $\delta z \simeq 3$ mm. The height of the detector δy can be increased considerably (~ 200 mm) as the divergence perpendicular to the diffraction plane does not affect the resolution, and the height is restricted primarily by the requirement not to cut the curving Debye rings at $2\theta_B \neq 90^\circ$. In TOF NSS, count rates are usually increased by using large arrays of detectors, covering horizontal and vertical angular ranges of about 30° . The TOF spectra recorded by each individual detector are transformed into a common d -spacing scale and added together in a single diffraction spectrum, in a process commonly known as electronic time focusing (Jorgensen *et al.*, 1989). Larger angular arrays are not feasible for NSS due to space and access requirements, and due to the increased uncertainty in the measured strain (Daymond, 2001).

Radial collimators made of thin absorbing blades (Withers *et al.*, 2000) are used to collimate the diffracted beam and ensure that all detectors look at exactly the same volume of the sample (Fig. 4*b*). The shape of the IGV and its dependence on the radial-collimator parameters can be calculated by simulations of the neutron trajectories (Wang *et al.*, 2000). The predicted intensity profile along the beam direction is triangular for the line passing through the focal point, and gradually becomes a Gaussian profile at increasing distances from this point. The FWHM of these distributions can be changed without altering the collimation α_{det}^z , by assembling blades of equal length at different distances from the focal point (l_c^1 and l_c^2 in Fig. 4*b*). Hence, a variable gauge volume can be achieved with two pairs of adjustable slits to define the incident-beam cross section, and a number of radial collimators of fixed collimation assembled at different distances from the focal point.

The previous calculations represent the ideal performance of slits and collimators. In practice, these may be affected by manufacturing details and by intensity variations across the beam, so the actual resolution should be determined experimentally.

From the present discussion, it follows that a precise definition of the IGV is a rather complex matter. For operational purposes, we define the IGV as a cuboid of sides Δx , Δy and Δz , so the illuminated gauge volume becomes $\delta V = \Delta x \Delta y \Delta z$. The dimensions of Δx and Δy are the FWHM values given by equation (10), and Δz is the width of the intensity profile seen from the collimators. For measurements performed near surfaces, the IGV may be only partially immersed within the specimen, and the effective centroid of the IGV differs from its geometrical centre. The sampled gauge volume (SGV) is the three-dimensional absorption weighted intersection between the IGV and the sample.

Finally, the uncertainty in the solid angle ascribed to the measured strain direction is given by the solid angle explored by the \mathbf{q} vectors of all individual detector elements. For a detector bank spread over relatively small angular ranges, $\Delta(2\theta_B)$ in the horizontal plane and $\Delta\phi$ out of this plane, the uncertainty in the \mathbf{q} direction is half of the detector's angular spread in the horizontal plane, and nearly equal to the angular

coverage out of this plane. This large angular coverage also means that even for a single diffraction peak, the actual number of crystallites sampled by a TOF diffractometer is much larger than those sampled on a reactor. This is because the angular $2\theta_B$ acceptance of a constant-wavelength neutron strain scanner is typically of the order of 0.1° , in comparison with the 20 – 30° range covered by a TOF detection bank.

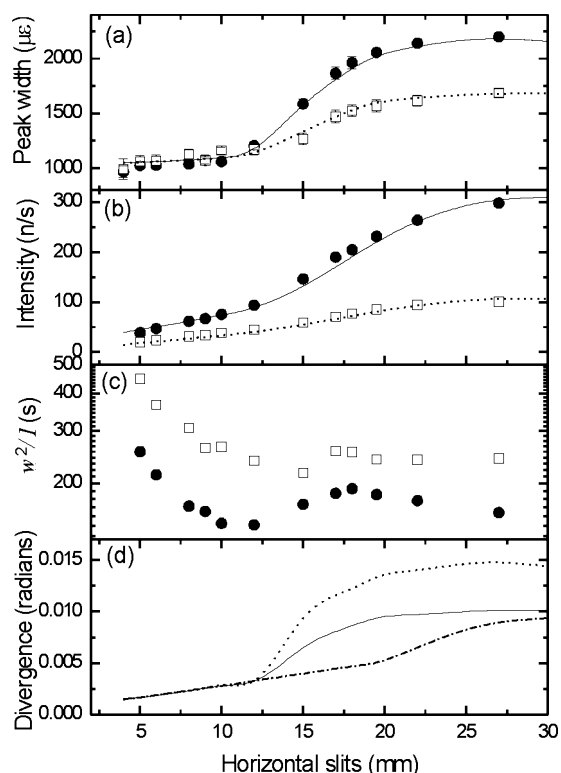
3. The ENGIN-X diffractometer

Following the requirements discussed above, ENGIN-X has been designed with a tuneable resolution and a variable gauge volume. This demanded novel solutions in terms of neutron optics and detector design, as described in this section.

The ISIS methane moderator was chosen for ENGIN-X due to its combination of narrow pulse width and high flux over the 1 – 3 Å wavelength range relevant to most engineering materials. After a comprehensive optimization, Johnson & Daymond (2002) showed that for this moderator the counting times are minimized with a primary flight path of ~ 50 m, and a diffracted beam with a horizontal divergence of 0.002 radians.

The neutrons are brought from the moderator to the sample position by means of neutron guides. Firstly, supermirror ($m = 2$) coated metal in the ISIS S8 primary beam shutter improves the uptake of neutrons from the moderator. Then a glass supermirror-coated neutron guide ($m = 3$, 60 mm high \times 25 mm wide) transports the neutrons to the sample position. From 4 m to 37.5 m from the moderator, the guide is curved in the horizontal plane with a radius of 5 km, away from the proton beam. This curvature improves the signal to noise ratio of the instrument by removing the high-energy neutrons and gamma rays produced during the spallation process. However, this also limits the minimum wavelength at the sample position to around 0.5 Å. A straight neutron guide from 37 m to 48.5 m, *i.e.* ending at 1.5 m before the sample position, removes any asymmetry in the neutron profile induced by the curved part of the guide.

The horizontal divergence of the beam, α_{in}^x , at the end of the neutron guide is ~ 0.005 radians \AA^{-1} , or ~ 5000 μe \AA^{-1} , clearly larger than the angular resolution specified in the design. Thus, both the horizontal and the vertical divergence of the incident beam can be adjusted with two sets of slits inserted in the straight part of the neutron guide, at 4 m and 1.5 m from the sample position, labelled s_4 and $s_{1.5}$, respectively. Figs. 5(*a*) and 5(*b*) show the effect of varying the slits' opening on the symmetric width and intensity of the 111 and 311 diffraction peaks measured on an AISI 306H stainless-steel sample. Both slits are opened by the same horizontal width, whilst the height is kept fixed at 45 mm. In both cases there is a sharp increase at 12.5 mm, *i.e.* when the opening corresponds to half of the guide width. The effect on counting time estimated with equation (3) is shown in Fig. 5(*c*). The instrument is optimized at somewhere between 12 and 15 mm. These experimental results were used to validate Monte Carlo simulations of the incident-beam optics performed with the software package *McStas* (Nielsen & Lefmann, 2000). Results of the simulations are shown by the solid and dotted lines in Figs. 5(*a*) and 5(*b*).


Figure 5

Performance of the ENGIN-X instrument for different apertures of the incident slits located at 1.5 and 4 m from the sample position. (a) and (b) show respectively the variation of the symmetric width and intensity of the 111 peak (solid symbols) and 311 peak (open symbols) measured for a stainless-steel sample. The lines are calculations made with a Monte Carlo model of the instrument. (c) The estimated counting time, showing a minimum around 12–15 mm. (d) The divergence of the incident beam at the sample position as given by the Monte Carlo simulations.

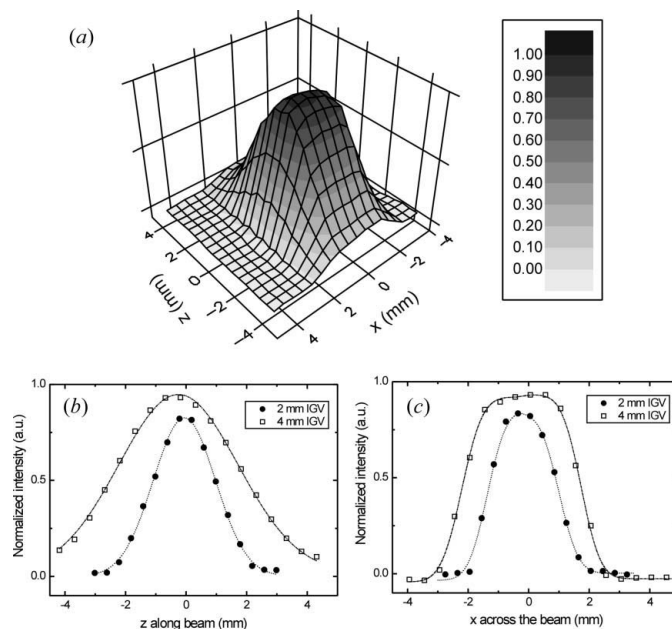
The calculated horizontal divergence of the incident beam at the sample position is shown by the solid and dotted curves in Fig. 5(d). A sharp increase in divergence is found at 12.5 mm. Inspection of the simulation results reveals that this increase is linked to the appearance of satellite peaks in the divergence distribution, complicating the tuning of the divergence. These satellite peaks disappear when the opening of $s_{1.5}$ is reduced, whilst still allowing a direct line of sight of the s_4 slit from the sample position. The dashed–dotted line in Fig. 5(d) shows the results of the simulations for an arrangement with $s_{1.5}$ (mm) = $s_4(1.5/4) + 2$ (mm) (now with s_4 in the abscissa). For this configuration, the divergence behaves linearly up to ~ 20 mm, where an increase in the slope is found, again, due to small satellite peaks.

The actual size of the IGV is defined by a set of motorized slits capable of producing a beam having a horizontal dimension of 0.3–10 mm, and a vertical dimension of 0.3–30 mm. These slits can be moved along a rail aligned to the beam direction, allowing change of the distance S_z to the sample between 0 and 120 mm. For small gauge volumes, these slits can also have a noticeable effect on the incident divergence (Santisteban, 2005).

ENGIN-X has two detector banks, centred at $2\theta_B = \pm 90^\circ$ to the incident beam and ~ 1.53 m from the IGV. The detector

banks cover $\pm 16^\circ$ in the horizontal plane and $\pm 21^\circ$ in the vertical plane. Each detector bank is made up of five units stacked vertically, each unit consisting of 240 scintillators. Each scintillator is 196 mm high by 3 mm wide, providing a horizontal angular resolution of ~ 0.002 radians. A new detector design was required in order to achieve this spatial resolution efficiently (Schooneveld & Rhodes, 2003). The detectors are made of $\text{ZnS}/^6\text{Li}$ scintillator material, coded *via* fibre optics to an array of photomultiplier tubes. Each bank covers a total detector area of 1.4 m^2 , which represents about 5% of the total 4π solid angle.

The dimension of the IGV along the beam is defined using radial collimators: a technology first designed and implemented on ENGIN (Johnson *et al.*, 1997). Whilst ENGIN used a single gauge dimension, ENGIN-X uses five sets of removable radial collimators providing 0.5, 1, 2, 3 and 4 mm gauge-width options. These sizes represent typical dimensions for spatial strain scanning experiments, as macroscopic strain distributions usually scale with the object size (Edwards & Santisteban, 2002). Additionally, the 4 mm gauge is ideal for real-time *in situ* studies, maximizing the IGV to reduce count times, whilst keeping the background low by eliminating neutrons scattered from sample-environment equipment. The collimator mounting system enables removal of a collimator to provide space for very bulky samples, with the sample still on the instrument.


Figure 6

(a) Shape of the ENGIN-X instrumental gauge volume, as measured by scanning a 0.25 mm thin nylon thread across the horizontal plane (xz plane in Fig. 4). (b) Intensity scans along the beam, *i.e.* across the collimators, for the 2 mm collimator (solid symbol) and for the 4 mm collimator (open symbol). The lines are Gaussian fits to the data. (c) Intensity scans across the beam along the line passing through the centre of the IGV for 2 mm and 4 mm opening of the horizontal slits. The lines are least-squares fits to the data using error functions to describe the edges.

Each radial collimator is composed of 160 vanes spanning 32° on the horizontal plane, assembled at different distances from the focal point. The vanes are 350 mm long and 50 μm thick, made of a 12 μm polyethylene foil covered by a paint containing gadolinium oxide particles. The collimators have l_c distances of 100, 160, 310, 400 and 490 mm, to provide the gauge sizes of 0.5, 1, 2, 3 and 4 mm, respectively. A horizontal cross section of the IGV for the 4 mm collimator is shown in Fig. 6(a), measured by horizontally scanning a 0.25 mm nylon thread across the beam. Line profiles for the 2 and 4 mm collimators along the beam direction, *i.e.* the z axis of Fig. 4(a), are shown in Fig. 6(b). Both profiles are properly fitted by Gaussian distributions, with widths of (2.05 ± 0.05) mm and (3.95 ± 0.05) mm, respectively. The profiles normal to the beam direction (*i.e.* along the x axis) are shown in Fig. 6(c). The edges of these distributions are well described by error functions with a broadening of 0.73 mm. The widths of these distributions, as given by the distance between the edges, were (2.3 ± 0.1) mm and (3.95 ± 0.05) mm, respectively.

The combined effects of these design features, along with the significant ($2\times$) increase in the detector solid angle, has resulted in a new instrument that greatly exceeds the performance of its predecessor, ENGIN. A demonstration of this is given by Fig. 7(a), which compares a cerium oxide (200) diffraction peak measured on ENGIN with its equivalent on ENGIN-X, normalized by the volume of the IGV. The gains of ENGIN over ENGIN-X can be quantified by the intensity and width of the peaks: the two parameters involved in the figure of merit. Fig. 7(b) shows the experimentally defined resolution of both instruments for the wavelength range of interest. As seen in the graph, on ENGIN-X the moderator and geome-

trical contributions are matched, whilst on ENGIN the moderator dictates the overall resolution. For ENGIN-X, a simple squares sum of moderator and geometrical contributions results in a nearly constant resolution of 1300 μe .

The gain in intensity is shown in Fig. 7(c). The curves correspond to the normalized count rate for a vanadium sample. The ENGIN-X incident-spectrum intensity is zero at short wavelengths due to the curvature of the neutron guide; the useable range is $\sim 0.5\text{--}6$ \AA . Overall, over an order of magnitude increase in intensity has been achieved on ENGIN-X. However, we note that for any single measurement, the wavelength range accessible to ENGIN-X is smaller than for ENGIN, even when both instruments look at the same moderator. This is because for ENGIN, located 16 m away from the moderator, all the wavelength range of interest is available with the 50 Hz pulse rate of the ISIS source; but this is no longer possible on ENGIN-X. Due to its 50 m flight path, at 50 Hz the usable wavelength window is reduced to just over 1.5 \AA . Thus, a slower pulse rate is required if wider wavelength ranges are to be exploited. In effect, the full range of the ENGIN-X spectrum displayed in Fig. 7(c) is only available with the instrument running at 12.5 Hz. This is accomplished on ENGIN-X by means of two sets of disc choppers located at 6 m and 9 m from the moderator. The frequency (50, 25, 16.7 and 12.5 Hz) and phase shift of the choppers relative to the neutron source pulse rate can be independently changed, providing great versatility for shaping the incident spectrum. In order to reduce the opening and closing time of the choppers, a novel design consisting of two counter-rotating discs was developed for this project (Galsworthy *et al.*, 2003).

Hence, the comparison between ENGIN and ENGIN-X

can be performed in either of two ways, based on the capability of the instruments to measure: (i) an individual peak or, (ii) all peaks within a predefined wavelength range. Fig. 7(c) compares the intensities of ENGIN and ENGIN-X for the latter case, with ENGIN-X running at 25 Hz, which is the optimal choice for macroscopic strain scanning in most engineering materials. We emphasize that only a user-selected 2.5 \AA interval of the displayed incident spectrum would be readily available at ENGIN-X at this pulse rate. Table 1 provides a more practical comparison between the performances of ENGIN-X (at 25 Hz) and ENGIN, in terms of the counting time taken by typical macroscopic strain scanning experiments in aluminium and steel samples. More than one order of magnitude decrease in counting times has been achieved. The experimental values given for the

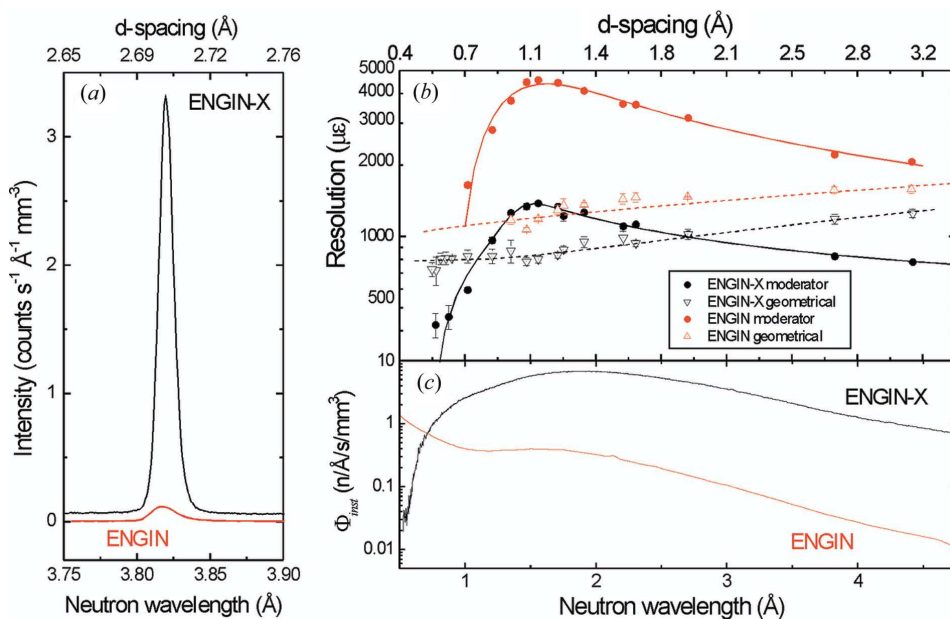


Figure 7 Comparison in performance between ENGIN-X and its predecessor ENGIN. (a) Ceria (200) diffraction peak as measured by both instruments. (b) Contributions to the instrument resolution: moderator (circles) and geometrical (triangles). In ENGIN-X, both component are matched over the complete wavelength range. (c) Gain in intensity: scattering spectra for a vanadium specimen. The fall of the ENGIN-X spectrum at low wavelength is due to the curvature of the neutron guide.

Table 1

Gain in performance in ENGIN-X over its predecessor ENGIN.

The table lists counting times for typical strain scanning and *in situ* loading experiments. Strain scanning times result from Rietveld refinement of the full diffraction pattern. *In situ* loading times require the five most intense reflections to be defined within a 50 $\mu\epsilon$ uncertainty.

Experiment type	ENGIN count time	ENGIN-X count time	Estimated count time for 50 $\mu\epsilon$	for 70 $\mu\epsilon$
Strain scanning, Al, 2 × 2 × 2 mm ³ gauge, 50 mm path length	1.3 h	5 min	8 min	4 min
Strain scanning, Fe, 2 × 2 × 2 mm ³ gauge, 14 mm path length	1.5–2 h	5 min	3 min	1.5 min
Strain scanning, Fe, 2 × 2 × 2 mm ³ gauge, 30 mm path length	5 h	20 min	21 minutes	11 min
Strain scanning, Fe, 4 × 4 × 4 mm ³ gauge, 60 mm path length	Impossible	1 h	1.5 h	48 min
<i>In situ</i> loading, 4 × 8 × 4 mm ³ gauge, Fe	1 h	1.5 min	1 min	
<i>In situ</i> loading, 4 × 8 × 4 mm ³ gauge, Ti	4.5 h	7 min	8 min	

spatial scanning results are rough estimates based on a 50 $\mu\epsilon$ uncertainty returned from a Rietveld refinement of diffraction data. For each category, measurements have been made on several different samples with various alloy contents and textures, with path lengths close to the values given; count times have been extrapolated to the conditions given. The ENGIN-X experimental times are compared with estimates described in the following section.

Finally, the ENGIN-X positioning table is capable of holding a sample weighing up to 1.5 tonnes. It can move the sample in the x , y , z and ω axes, with ranges of ± 250 mm in x and y , 700 mm in z , and 370° in ω , with a nominal accuracy of 10 $\mu\text{m}/100$ mm for a 0.5 tonne sample. In order to measure materials under applied loads, an *in situ* 100 kN hydraulic stress rig is also available on ENGIN-X, of identical design to that described by Daymond & Priesmeyer (2002). The sample temperatures can range from room temperature to 1273 K within atmosphere or inert gas using a radiant furnace (Daymond & Withers, 1996). Table 1 also lists typical gains in performance achieved by ENGIN-X for *in situ* loading experiments. For this case, the data collection times correspond to the five most intense first-order peaks in a randomly textured material, measured to 50 $\mu\epsilon$ uncertainty.

4. Counting times on a TOF strain scanner

A reliable estimation of experimental counting times for other materials, geometries and spatial resolutions than those given in Table 1 would be very useful in assessing the feasibility of specific experiments on a TOF strain scanner. Besides this, it would enable an efficient use of the limited experimental time by allowing the optimization of the count times at each measurement position, as recently discussed for constant-wavelength diffractometers by Withers (2004).

An estimation of the counting time required for a desired strain precision was given in equation (3). For many engineering specimens, the sample-induced broadening is small and the peak width is dominated by the instrument resolution, hence the count times are effectively dictated by the peak count rate, *i.e.* equation (6). Although useful for instrument design purposes, for experimental design it is convenient to group all the instrument-dependent parameters in equation (6) into a single factor, Φ_{instr} .

$$I_{hkl} = \Phi_{\text{instr}} P_{hkl} \exp(-l\mu_{hkl}) \delta V, \quad (11)$$

giving the peak intensity in terms of only four contributions. Φ_{instr} is a wavelength-dependent factor containing the incident neutron flux, the efficiency and the solid angle of the detection bank. This term is strongly instrument-dependent, so interpolation of an experimental look-up table is the easiest way to determine it. The Φ_{instr} functions for ENGIN-X and ENGIN are presented in Fig. 7(c). The wavelength dependence of Φ_{instr} was defined by measuring a vanadium sample (assuming it is a perfectly elastic incoherent scatterer), whilst the scaling factor was obtained from reference Fe and Al specimens. The factor P_{hkl} depends on the material. The experimental counting rates for a series of technologically relevant materials are shown in Fig. 8(a), together with the values calculated using equation (11). The reported count rate corresponds to a 1 mm³ gauge volume, located 1 mm under the surface of the specimen, measured on powder specimens. The agreement between experimental and calculated values is very good, varying over almost three orders of magnitude. The count rate in actual engineering specimens will be somewhat different, due to the higher density of solid specimens and the likely presence of texture.

The third factor affecting the count rate is the attenuation of the neutron beam within the specimen. Fig. 8(b) shows such a decrease in peak intensities, in this case for the line CC' of the stainless-steel specimen described in the next section. The attenuation in all three peaks is well described by least-squares fits with an exponential decay law, but with slightly different attenuation coefficients: $\mu_{111} = (0.119 \pm 0.03) \text{ cm}^{-1}$, $\mu_{200} = (0.106 \pm 0.03) \text{ cm}^{-1}$, $\mu_{220} = (0.111 \pm 0.02) \text{ cm}^{-1}$. These differences are due to the dependence of the total material cross section on neutron wavelength. A diffraction peak measured on a TOF diffraction bank contains contributions from neutrons from a range of wavelengths, from $\lambda_{\text{min}} = 2d_{hkl} \sin \theta_{\text{min}}$ to $\lambda_{\text{max}} = 2d_{hkl} \sin \theta_{\text{max}}$, where θ_{min} and θ_{max} are the minimum and maximum Bragg angles in the detector bank. The material attenuation coefficient is given by $\mu = N\sigma_{\text{tot}}$, with N the number of atoms per unit volume and σ_{tot} the material's microscopic total cross section. The total cross section of polycrystalline materials has a highly complex dependence on neutron wavelength; however, the attenuation coefficient μ_{hkl} for a particular reflection can be calculated by

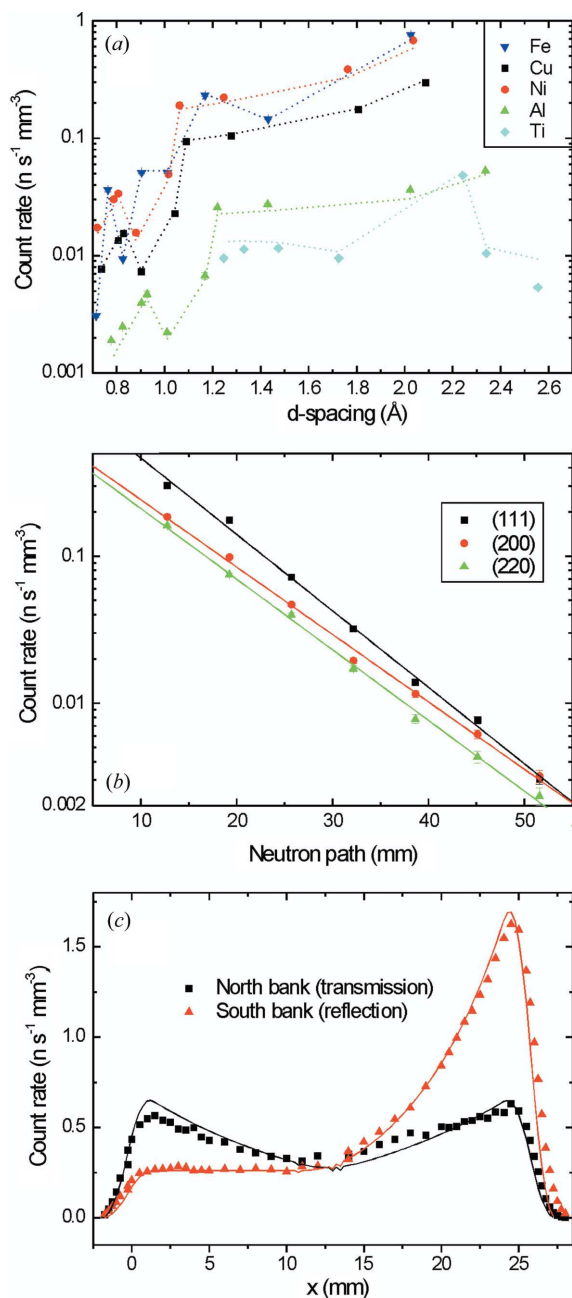


Figure 8 Factors affecting count rate in a neutron strain scanning experiment. (a) Integrated count rate for selected peaks of powders of common structural materials. The count rate is for a 1 mm³ gauge volume 1 mm under the surface of the specimen. The solid symbols correspond to experiments performed on the ENGIN-X instrument. The lines are the values predicted by equation (11). The experimental uncertainty is smaller than the symbols. (b) Attenuation of the beam as a function of the neutron path inside the specimen. The graph shows the integrated peak intensity for selected reflections. The lines are least-squares fits to the data using an exponential decay law. (c) Measured and simulated count rates for a line scan across a 25 mm cube filled with iron powder.

averaging the total cross section over the associated wavelength range (Wang *et al.*, 2001):

$$\mu_{hkl} = N \frac{\int_{2d_{hkl} \sin \theta_{\min}}^{2d_{hkl} \sin \theta_{\max}} \sigma_{\text{tot}}(\lambda) d\lambda}{2d_{hkl}(\sin \theta_{\max} - \sin \theta_{\min})}. \quad (12)$$

Equation (12) for stainless steel gives $\mu_{111} = 0.1164 \text{ cm}^{-1}$, $\mu_{200} = 0.1069 \text{ cm}^{-1}$ and $\mu_{220} = 0.1113 \text{ cm}^{-1}$, agreeing well with the measured values. This variation in the attenuation coefficient should be accounted for when estimating counting times deep in specimens. For instance, due to this variation, the count rate of the 111 peak is 75% larger than that of 200 for a neutron path of 12 mm, but both peaks have essentially the same count rate for a 52 mm path length. It is worth noting that the attenuation coefficient μ_{hkl} depends on texture through the total cross section.

The last factor that may affect the peak intensities is the partial filling of the IGV, particularly for scans near the surface of a specimen. Based on the description of the IGV in §2.3, the count rate near a surface can be calculated by replacing δV in equation (11) by the SGV $\delta V'$, corresponding to the intersection between the IGV and the sample. Fig. 8(c) shows an intensity profile for a line scan across a 25.4 mm cube filled with iron powder, together with calculated values. The good agreement between the experiment and the simulated values supports the use of a cuboid to describe the IGV in intensity calculations, instead of the more complex distributions presented in Fig. 6.

Thus, we can estimate the counting time required to measure the position of a single diffraction peak on ENGIN-X with a resolution $\delta\varepsilon$:

$$T = \frac{[(\delta_\varepsilon t_{hkl})^2 + (\delta_\varepsilon d_{hkl})^2]}{(\delta\varepsilon)^2} (\Phi_{\text{instr}} P^{hkl})^{-1} \frac{\exp(l\mu_{hkl})}{\delta V}. \quad (13)$$

In practice the utility of equation (13) will be limited by the presence of any texture. Moreover, in TOF neutron strain scanning experiments, the value of the macroscopic strain is obtained from the analysis of all the peaks appearing within the accessible wavelength range. That is, the average strain across all the crystallites sampled by a TOF experiment is derived from the variation of the crystallographic lattice parameters, obtained from a Rietveld or Pawley least-squares refinement of the full diffraction pattern (Daymond *et al.*, 1997; Daymond, 2004). The effect of measuring more than one peak is effectively to lower the uncertainty in the experimental strain, hence reducing counting times (Johnson & Daymond, 2002),

$$T = \frac{(\delta_\varepsilon t + \delta_\varepsilon d)^2}{(\delta\varepsilon)^2} \left(\sum_{hkl} I_{hkl} \right)^{-1}, \quad (14)$$

where the sum is over all the hkl peaks accessible to the experiment, and we have assumed that the resolution of an optimized TOF diffractometer is nearly constant ($\delta_\varepsilon t_{hkl} = \delta_\varepsilon t$).

Predicted counting times using equations (13) and (14) are compared with the corresponding experiments in Table 1, using strain uncertainties of 50 $\mu\varepsilon$ and 70 $\mu\varepsilon$ for spatial scanning; and requiring the five most intense peaks to be defined within 50 $\mu\varepsilon$ for *in situ* loading. For both types of experiment, the estimated counting times agree well with the predictions from equations (13) and (14). All counting times were calculated assuming a constant instrument resolution $\delta_\varepsilon t_{hkl} =$

Table 2

Estimated counting times (min) for strain measurements on ENGIN-X with an uncertainty of 50 $\mu\epsilon$.

For each material, the estimated times are those obtained from the position of the most intense reflection, and from the lattice parameters resulting from a Rietveld refinement of the complete diffraction pattern.

	Gauge volume $2 \times 2 \times 2 \text{ mm}^3$				Gauge volume $4 \times 4 \times 4 \text{ mm}^3$			
	Penetration (mm)							
	2	10	20	30	4	20	40	50
Al (111)	16.4	17.8	19.7	21.8	2.1	2.5	3	3.3
Al Rietveld	5.9	6.4	7.1	7.8	0.8	0.9	1.1	1.2
F.c.c. Fe (111)	2.1	5.3	17	54.5	0.3	2.1	21.8	70
F.c.c. Fe Rietveld	0.9	2.2	6.5	19.7	0.1	0.8	7.4	22.5
B.c.c. Fe (110)	1.4	3.5	10.9	34.1	0.2	1.4	13.3	41.5
F.c.c. Fe Rietveld	0.9	2.1	6.1	18.3	0.1	0.8	6.8	20.4
Ni (111)	2	11	91.4	761.1	0.4	11.4	792.2	6595.8
Ni Rietveld	0.9	4.2	31.5	233.4	0.2	3.9	216.2	1602.9
Cu (111)	3.1	7.4	21.7	63.8	0.5	2.7	23.5	69
Cu Rietveld	1.3	2.9	7.9	21.1	0.2	1	7.1	19.3
Zr (101)	4.5	5	5.7	6.5	0.6	0.7	0.9	1.1
Zr Rietveld	1.5	1.6	1.9	2.2	0.2	0.2	0.3	0.4
Ti (101)	17.9	34.1	76.5	171.6	2.6	9.6	48.1	108
Ti Rietveld	6.5	11.4	23.1	46.7	0.9	2.9	11.8	24

1300 $\mu\epsilon$ and a sample broadening $\delta_\epsilon d_{hkl} = 100 \mu\epsilon$. Predictions for other materials and depths are presented in Table 2. The predicted counting times are for 50 $\mu\epsilon$ strain accuracy on ENGIN-X running at 25 Hz, using gauge volumes of $2 \times 2 \times 2 \text{ mm}^3$ and $4 \times 4 \times 4 \text{ mm}^3$. In general, the counting times for the full-pattern analysis are better estimates of the actual experimental times, as the total count rate is less sensitive to the presence of texture.

We note that equation (13) is only correct for an isolated peak with no background. In the presence of a non-negligible background level, the time T required to achieve the same strain accuracy increases by the penalty factor $[1 + 2(2^{1/2})b/h_{hkl}]$, where h_{hkl} is the height of a Gaussian peak and b is the background level (Withers *et al.*, 2001; Withers, 2004). The factor of $2(2^{1/2})$ in this expression is replaced by slightly different factors for non-Gaussian peak shapes (Withers *et al.*, 2001). This correction will be important for materials with a very large incoherent scattering cross section, or for measurements performed deep within a specimen. For the materials listed in the table, the effect of incoherent scattering is only significant for titanium, where b/h_{hkl} for the 10 $\bar{1}$ 1 peak is 0.05, and is even larger for the other reflections. On the other hand, the increasing importance of background at larger depths is due to the contribution of multiple scattered neutrons mainly within the sample. We have experimentally found that the background level is about a third of the peak height for $4 \times 4 \times 4 \text{ mm}^3$ of stainless steel at a depth of 50 mm. Due to the complex nature of the TOF peak shape, and the fact that the background varies as a function of wavelength, a more quantitative description of the influence of background in TOF diffractometers on count times is beyond the scope of this work.

5. The ENGIN-X virtual laboratory

In parallel with the optimization of the neutron optics, improvements in sample positioning have been achieved by

using detailed three-dimensional models of the samples, and a pair of theodolites for precise alignment on the instrument. However, computing help is essential for full exploitation of these advances in instrumentation, as well as to monitor the experimental progress and results. Otherwise measurements would be made in a conservative manner, and the final information gathered would be less than could be optimally achieved. With this in mind, the processes of planning, alignment and data analysis have been simplified by writing *SSCANSS* (James *et al.*, 2002; James *et al.*, 2004), a computer program that: (i) provides computer aids in setting up the initial measuring strategy, (ii) automates sample alignment and all routine aspects of the measurement process, (iii) provides data analysis in near real-time, allowing decisions on changes to the measurement strategy.

These requirements have been achieved by the creation of a 'virtual laboratory', *i.e.* a three-dimensional representation of the laboratory and the sample that can be easily manipulated through a graphical user interface, as shown in Fig. 9. The three-dimensional model of the laboratory includes the collimators, the slits and the positioning table, with the IGV at the centre of the laboratory system. The dimensions of the IGV can be changed by changing the slit apertures and collimators. The three-dimensional model of the sample can be produced within the program from basic primitive objects (cuboids, cylinders, pipes, *etc.*), exemplified by the simple model used in Figs. 9(a) and 9(c) to describe the 190 kg pipe shown in place in the instrument in Fig. 9(b). For more complex shapes or regions requiring improved spatial resolution, a precise three-dimensional model can be created using a coordinate-measuring machine (CMM), also available on the ENGIN-X facility. Fig. 9(d) shows such a model for the region of interest of the pipe, *i.e.* in the vicinity of a weld repair. The ENGIN-X CMM is an LK HC-90 model provided with a Metris laser head for fast scanning of large samples. The measurement zone of the CMM limits a single measurement scan to around $0.5 \times 0.5 \times 1 \text{ m}$; however, multiple overlapping scans can be

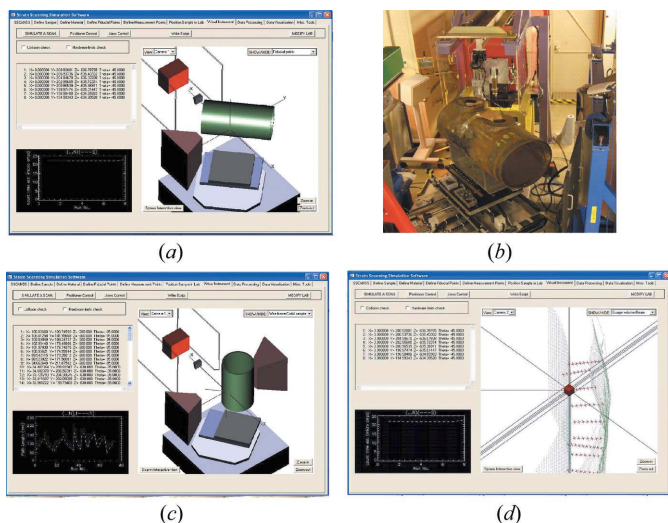


Figure 9
The ENGIN-X virtual laboratory. Three-dimensional models of the laboratory and sample are used for planning of experiments, in this case to measure the axial (a) and radial (c) directions of the strain tensor of the 190 kg pipe shown in (b). The three-dimensional model of the sample is produced either from simple primitive objects, such as in (a) and (c), or from detailed descriptions of the actual surface of the specimen (d) using the ENGIN-X coordinate-measuring machine. The precise alignment of the sample in the laboratory (both real and virtual) is achieved using two theodolites.

built up to deal with larger objects. The resolution of the laser scanner in determining the position of a single point in a surface is around 5 μm , but a smoothly varying surface can be defined to a substantially better accuracy than this. Alternatively, the sample model can be imported from external computer-aided design (CAD) software packages. The SSCANSS package is written in IDL (Research Systems, 2004); the implementation also makes use of the *Open Genie* software suite (Moreton-Smith *et al.*, 1996).

5.1. Experiment planning

The points to be measured are defined interactively in a graphical visualization of the sample. To do so, the program presents cross sections of the specimen where the points of interest can be selected using a mouse. Alternatively, the measurement points can be defined by importing their (x, y, z) coordinates in the sample system. The crosses displayed in Fig. 9(d) represent a complete scan to be performed during the experiment.

Different sample orientations provide different components of the strain tensor. The program allows the exploration of alternative experimental arrangements, and provides warnings in case of collisions. The effects of beam attenuation for each configuration are easily explored by rotating the sample in the virtual laboratory, as shown in Figs. 9(a) and 9(c) for the axial and radial strain components, respectively. The program can also provide the estimated counting time expected for each orientation using the expressions introduced in the previous section.

5.2. Sample alignment

In ENGIN-X, the positioner movements required to bring samples of arbitrary complexity to the correct position for measurement may be generated automatically. This facility requires the determination of the transformation that relates the measurement positions in the sample and laboratory coordinate systems. This transformation is expressed in terms of a 4×4 matrix, \mathbf{S} , in homogeneous coordinates. The use of homogeneous coordinates (Foley *et al.*, 1997) is standard in many areas of computer modelling and is convenient as it allows translation, which must normally be represented by an addition, to be represented by a matrix multiplication. In order to determine \mathbf{S} , the positions of a number of fiducial points on the surface of the sample are measured using a pair of theodolites. A least-squares procedure is then used to find the transformation matrix that most closely maps the fiducial points on the sample to their measured positions in the laboratory. Since the sample is a rigid body, a minimum of three non-collinear fiducial points are sufficient for this purpose, though using a larger number may improve accuracy. The transformation matrix so determined provides the position of the sample corresponding to the initial position of the ENGIN-X positioning table, which is described by a further transformation matrix \mathbf{P} . It follows that if the positioner were now moved to $(x = y = z = \omega = 0)$, the sample position would be given by the transformation $\mathbf{S}_0 = \mathbf{P}^{-1}\mathbf{S}$. The transformation matrix, \mathbf{S}_i , for any subsequent table position may now be calculated as

$$\mathbf{S}_i = \mathbf{P}_i\mathbf{P}^{-1}\mathbf{S} = \mathbf{P}_i\mathbf{S}_0, \quad (15)$$

where \mathbf{P}_i is the transformation matrix describing the new position of the table.

Since the angular orientation of the positioning table is generally prescribed by the requirement that a particular strain component be measured, the matrix \mathbf{P}_i is unique and is determined by the translation needed to bring the required measurement point to the gauge volume.

The alignment procedure described above is purely optical insofar as no reference is made to the position of the neutron beam. As a check of the position of the sample with respect to the beam, and in order to take account of slight beam misalignments, the diffracted beam intensity is measured as entrance/exit scans are performed. The experimental intensity profile can be used to estimate the location of the surface of the sample, or, alternatively it may be compared directly with a SSCANSS predicted profile, such as the solid lines shown in Fig. 8(c). Any discrepancy due to beam misalignment is then incorporated into SSCANSS as an offset, enabling the scan to proceed as previously defined.

The theodolites are placed at beam height. One of theodolites makes an angle of 135° with the incident beam, *i.e.* is aligned to \mathbf{q}_2 in Fig. 1, and the other is more arbitrarily positioned, making an angle of approximately 30° . The models of the sample, the laboratory and the transformation matrices are attached to the experimental data files for a precise recon-

struction of the instrumental arrangement for inspection and analysis at a later stage.

5.3. Experiment execution and data analysis

Provided with the transformation between sample and laboratory coordinate systems, the program can drive the positioning table in order to visit all of the points within the scan. At each measurement position, the spectra recorded by the individual detectors are time-focused, as described above. The program provides automatic single-peak and full-pattern refinement of the diffraction spectra specially devised for strain determination, through a library of common engineering materials. This enables researchers who are not experts in crystallography to keep pace with the experiment, and to be able to modify the experimental plan in the light of experience gained during earlier parts of the measuring process. Single-peak fits use a peak profile consisting of the convolution of a truncated exponential with a Voigt function. Full-pattern refinements use the computer code *GSAS* (Von Dreele *et al.*, 1982). As most samples are textured, the refinement is performed leaving the peak intensities unconstrained, as described by Pawley (1981). To ensure the convergence of the refinement, initial guesses of the lattice parameters are obtained from single-peak refinement of the most intense peak.

The program can calculate the centroid of the SGV (as given by the geometric approximation of §2.3) and display the IGV in a three-dimensional representation of the sample, as well as provide the actual direction of the measured strain in the sample coordinate system.

5.4. Example

We briefly describe a case study, namely a map of the elastic strain near a repair weld, in order to illustrate the new capabilities that ENGIN-X and *SSCANSS* have opened within this field. Repair welds are introduced into structures either to remedy initial fabrication defects found by routine inspection, or to rectify in-service degradation of components. We have worked in collaboration with British Energy to determine the residual stresses in repair welds in large components (Bouchard *et al.*, 2005). A typical example is the repair-welded component shown in Fig. 9(b), and schematically depicted in Figs. 10(a) and 10(b). The pipe was fabricated by manual metal arc welding of two ex-service 316H stainless-steel power-station steam headers. In order to study the effect of a typical repair process, a section of the original weld was removed, and subsequently filled with new material using the same process. Scans of the full strain tensor were performed along lines BB' and CC' at the middle and end of the heat-affected zone (HAZ) of the repair; and along lines DD' and EE' on equivalent locations on the original weld. In addition, we measured maps of the axial strain on the planes containing these lines. Critical to this work has been the use of laser CMM scanned models within *SSCANSS*, allowing manipulation of the virtual model for a detailed pre-planning of the experiment. A visual representation of the measurement positions is

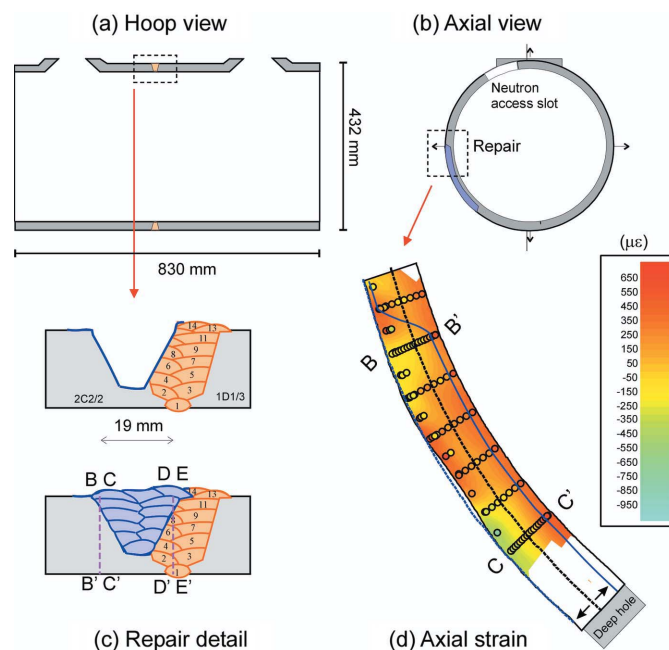


Figure 10 Strain mapping in a repaired weld on a steam header (Bouchard *et al.*, 2005). (a) Schematic diagram of the original pipe, produced by manual arc butt welding of two ex-steam-headers. (b) Axial and (c) hoop views of the repair introduced in the weld. A section of the original weld was removed, and subsequently filled with new material. (d) Axial strain mapped on plane $BB'CC'$ in the heat-affected zone of the repair. The symbols indicate the locations and values of the actual measurements. The profile of the cross section was produced using a coordinate-measuring machine.

shown in Fig. 9(d). Before the development of the *SSCANSS* software, setting up large complex specimens could take days of beam time and the calculation of beam exposure times was a hit or miss affair based on experience.

A map of the measured axial strain in the HAZ of the repair is shown in Fig. 10(d). The map reveals two main concentrations of tensile strain beneath the outer surface of the pipe at the stop-end and about midway between BB' and CC' . These short-range stress concentrations revealed the importance of stop-end effects for a correct description of the repair process. Each point was measured for 7 min, so the full map was completed in about 7 h. Considering only exposure times, a similar map on ENGIN would have taken nearly a week. The detailed information provided by the axial strain maps would not have been accessible in a reasonable time scale for such a large industrially relevant component before ENGIN-X.

6. Conclusions

In this paper we have described ENGIN-X, an instrument that represents the current state-of-the-art for NSS, which has been specifically designed to perform measurements of interplanar distances at precise locations within bulky specimens as fast as possible. Two very different aspects of the instrument have been separately optimized. Firstly, the neutron optics was designed using a figure of merit that describes the effect of all instrumental parameters on counting times, and a flexible

definition of gauge volumes and divergence was provided. Secondly, the routine operation of the instrument was optimized by including ancillary hardware (theodolites, CMM), in combination with a three-dimensional computer representation of the instrument.

Examples of the reduction in counting times between ENGIN-X and its predecessor ENGIN, as a result of the optimized neutron optics, have demonstrated improvements in performance between 15× and 40×. The variation in performance results from qualitative differences between experiments, as in NSS we are mainly interested in the average response of the material, whilst for *in situ* loading we are concerned with shifts of the individual peaks. The improvements in neutron optics have been presented in Fig. 7, which compares the count rates and peak widths of ENGIN-X and ENGIN. The theoretical improvements in counting time of ENGIN-X over ENGIN can be calculated with equation (3). For an experiment where we were only interested in the position of a single diffraction peak, ENGIN-X could run at a 50 Hz pulse rate and the reduction in counting would be up to 100×. However, in practice ENGIN-X must run at a lower pulse rate (typically 25 Hz) in order to measure the position of several peaks. Due to the opening and closing times of the choppers, the actual TOF range accessible with ENGIN-X operating at lower pulse rates is smaller than the nominal TOF period, so the 40× improvement observed for *in situ* loading is reasonable. For strain scanning, such counting time estimates are not straightforward, as the uncertainty comes from a Rietveld refinement of the diffraction data. Nevertheless, the counting times reported in Table 1, estimated by including the contribution from all peaks within the available TOF range, agree quite well with the experimental times. For this case, the typical reductions in counting times for ENGIN-X running at 25 Hz are ~20×.

Strain measurements performed on TOF neutron strain scanners are sometimes compared or combined with experiments performed on constant-wavelength strain scanners (Stelmukh *et al.*, 2002). Therefore, in this paper we have paid special attention to presenting absolute values for the experimental count rates, properly normalized by the instrumental gauge volume to allow comparison between the techniques. It must be noted, however, that a proper evaluation of the instrument performance cannot be based on count rates or resolution only, but on the ability to tackle specific problems in strain analysis. Consider for example the case of NSS in nickel, as a direct comparison can be performed with Ni powder data measured at a constant-wavelength strain scanner at Chalk River, Canada (Browne, 2001). The reported count rate for the 311 reflection ($0.4 \text{ counts s}^{-1} \text{ mm}^{-3}$) is about twice the count rate for the same reflection measured on ENGIN-X running at 25 Hz, but only a fourth of the added count rate including all available reflections ($1.6 \text{ counts s}^{-1} \text{ mm}^{-3}$). Considering that the resolution of the instrument used in that work ($\sim 2500 \mu\epsilon$) is about twice that of ENGIN-X ($\sim 1300 \mu\epsilon$), and that two strain directions can be measured simultaneously in ENGIN-X, we estimate a ~12× reduction in counting times. Even larger improvements are achieved for materials

with longer d spacings. For instance, measuring the (0002) planes for zirconium alloys requires an incident wavelength of 3.6 \AA (at $2\theta_B \simeq 90^\circ$), readily available on ENGIN-X, but not available at constant-wavelength strain scanners. As a result, the (0004) planes are studied instead, which results in an order of magnitude decrease in the diffracting power of the material.

In addition to the gains in count rates, ENGIN-X allows a very flexible definition of the IGV and the incident-beam divergence. In particular, we have discussed how the divergence can be tuned for samples presenting very broad peaks, and its effect on the shape and size of the IGV. We have confirmed that, for operational purposes, the gauge volume can be effectively represented as a cuboid having sides defined by the height, width and position of the three pairs of slits.

The improvements achieved by the development of the ENGIN-X virtual laboratory software are more difficult to quantify. However, the impact has been evident in two areas: (i) it has allowed novice users to perform strain scanning experiments successfully with little training time, and (ii) it has opened the possibility of more complex scans and improved spatial mapping experiments. For instance, the strain map reported here would not have been practically possible on ENGIN, not only because of the long experimental times involved, but also due to the complexity of positioning the gauge volume at precise locations below a highly irregular surface. Another contribution of the SSCANSS virtual laboratory has thus been in the calculation of the centroid of the SGV for measurements performed near surfaces, allowing a precise definition of the measurement position.

The maximum accessible depth is an important feature of a neutron strain scanner. On ENGIN-X, the maximum path lengths measured so far are 60 mm in stainless steel (Hossain *et al.*, 2006), 60 mm in nickel superalloys (Rist *et al.*, 2006) and 220 mm in aluminium. An approximate estimation of the maximum depth achievable for other materials for a given set of strain uncertainty, gauge volume and maximum counting time can be inferred from Table 2. For more precise estimations, the sample texture, the attenuation coefficient, the peak width, and the background rate should all be properly defined. At present, the easiest way to do this is still to perform a test measurement prior to the actual experiment.

As a result of all these improvements in performance, maps of the elastic strain in irregular bulky specimens (1–1000 kg) can be easily measured with ENGIN-X within several hours.

The authors would like to thank Ed Oliver and Jude Dann for their help during much of the experimental work, Mike Johnson for guidance and support, Dave Maxwell for technical assistance, and John Bouchard for kindly allowing the publication of the results on the repaired pipe. This work has been funded by an EPSRC grant and CCLRC grant No. GR/M51963.

References

- Allen, W., Andreani, C., Hutchings M. T. & Windsor, C. G. (1985). *Adv. Phys.* **34**, 445–473.

- Bouchard, P. J., George, D., Santisteban, J. R., Bruno, G., Dutta, M., Edwards, L., Kingston, E. & Smith, D. J. (2005). *Int. J. Pressure Vessels Piping*, **82**, 299–310.
- Browne, P. A. (2001). PhD thesis, University of Salford, UK.
- Buras, B. (1963). *Nukleonika*, **8**, 259–260.
- Daymond, M. R. (2001). *Physica B*, **301**, 221–226.
- Daymond, M. R. (2004). *J. Appl. Phys.* **96**, 4263–4272.
- Daymond, M. R., Bourke, M. A. M., Von Dreele, R. B., Clausen, B. & Lorentzen, T. (1997). *J. Appl. Phys.* **82**, 1554–1562.
- Daymond, M. R. & Edwards, L. (2004). *Neutron News*, **15**, 24–28.
- Daymond, M. R., Johnson, M. W. & Sivia, D. S. (2001). *J. Strain Anal.* **37**, 73–85.
- Daymond, M. R. & Priesmeyer, H. G. (2002). *Acta Mater.* **50**, 1613–1626.
- Daymond, M. R. & Withers, P. J. (1996). *Scr. Met.* **35**(6), 717–720.
- Edwards, L. & Santisteban, J. R. (2002). *Appl. Phys. A Mater. Sci. Process.* **74S**, 1424–1426.
- Fitzpatrick, M. E. & Lodini, A. (2003). *Analysis of Residual Stress by Diffraction using Neutron and Synchrotron Radiation*. London: Taylor and Francis.
- Foley, J. D., van Dam, A., Feiner, S. K. & Hughes, J. F. (1997). *Computer Graphics: Principles and Practice, in C*. New York: Addison Wesley.
- Galsworthy, P., Abbley, D., Bowden, Z. A., Brind, M. S., Lay, S. & Wakefield, S. (2003). *Proc. ICANS XVI*, Vol. 1. ISSN 1433-559X.
- Hossain, S., Truman, C. E., Smith, D. J. & Daymond, M. R. (2006). *Int. J. Mech. Sci.* **48**, 235–243.
- Hutchings, M. T., Withers, P. J., Holden, T. M. & Lorentzen, T. (2005). *Introduction to the Characterization of Residual Stress by Neutron Diffraction*. Boca Raton: CRC Press, Taylor and Francis.
- Ikeda, S. & Carpenter, J. M. (1985). *Nucl. Instrum. Methods A*, **239**, 536–544.
- ISO/TTA 3:2001 (2001). *Polycrystalline Materials – Determination of Residual Stresses by Neutron Diffraction*. International Organization for Standardization.
- James, J. A., Santisteban, J. R., Daymond, M. R. & Edwards, L. (2002). Proc. NOBUGS2002, NIST, Gaithersburg, USA, <http://arXiv.org/abs/cond-mat/0210432>.
- James, J. A., Santisteban, J. R., Daymond, M. R. & Edwards, L. (2004). *Physica B*, **350**, E743–E746.
- Johnson, M. W. & Daymond, M. R. (2002). *J. Appl. Cryst.* **35**, 49–57.
- Johnson, M. W., Edwards, L. & Withers, P. J. (1997). *Physica B*, **234**, 1141–1143.
- Jorgensen, J. D., Faber, J. Jr, Carpenter, J. M., Crawford, R. K., Haumann, J. R., Hitterman, R. L., Kleb, R., Ostrowski, G. E., Rotella, F. J. & Worlton, T. G. (1989). *J. Appl. Cryst.* **22**, 321–333.
- Kamminga, J. D., De Keijser, T. H., Mittemeijer, E. J. & Delhez, R. (2000). *J. Appl. Cryst.* **33**, 1059–1066.
- Moreton-Smith, C. M., Johnston, S. & Akeroyd, F. A. (1996). *J. Neutron Res.* **4**, 41–47.
- Nielsen, K. & Lefmann, K. (2000). *Physica B*, **283**, 426–432.
- Pawley, G. S. (1981). *J. Appl. Cryst.* **14**, 357–361.
- Research Systems Inc. (2004). Interactive Data Language Version 6.1. (<http://www.itvision.com/idl>.)
- Rist, M. A., Tin, S., Roder, B. A., James, J. A. & Daymond, M. R. (2006). *Met. Mater. Trans. A*, **37A**, 459–467.
- Santisteban, J. R. (2005). *J. Appl. Cryst.* **38**, 934–944.
- Schooneveld, E. M. & Rhodes, N. J. (2003). *Proc. ICANS XVI*, Vol. 1, pp. 251–258. ISSN 1433-559X.
- Snyder, R. L., Fiala, J. & Bunge, H. J. (1999). *Defects and Microstructure Analysis by Diffraction*. Oxford University Press.
- Stelmukh, V., Edwards, L., Santisteban, J. R., Ganguly, S. & Fitzpatrick, M. E. (2002). *Mater. Sci. Forum*, **404–407**, 599–604.
- Von Dreele, R. B., Jorgensen, J. D. & Windsor, C. G. (1982). *J. Appl. Cryst.* **15**, 581–589.
- Wang, D. Q., Santisteban, J. R. & Edwards, L. (2001). *Nucl. Instrum. Methods A*, **460**, 381–390.
- Wang, D. Q., Wang, X. L., Robertson, J. L. & Hubbard, C. R. (2000). *J. Appl. Cryst.* **33**, 334–337.
- Webster, G. W. (2000). Editor. *VAMAS Report 38*. ISSN 1016-2186.
- Windsor, C. G. (1981). *Pulsed Neutron Scattering*. London: Taylor and Francis.
- Withers, P. J. (2004). *J. Appl. Cryst.* **37**, 596–606.
- Withers, P. J., Daymond, M. R. & Johnson, M. W. (2001). *J. Appl. Cryst.* **34**, 737–743.
- Withers, P. J., Johnson, M. W. & Wright, J. S. (2000). *Physica B*, **292**, 273–285.